LAWRENCE
LIVERMORE
NATIONAL
LABORATORY

LLNL-JRNL-668328

Equations of State of Anhydrous AlF3 and AlI3: Modeling of Extreme Condition Halide Chemistry

E. Stavrou, J. M. Zaug, S. Bastea, J. C. Crowhurst, A. F. Goncharov, H. B. Radousky, M. R. Armstrong, S. K. Roberts, J. W. Plaue

March 11, 2015

Journal of Chemical Physics

Disclaimer

Equations of State of Anhydrous AlF_3 and AlI_3: Modeling of Extreme Condition Halide Chemistry

Elissaios Stavrou,[1, 2, a)] Joseph M. Zaug,[2, b)] Sorin Bastea,[2] Jonathan C. Crowhurst,[2] Alexander F. Goncharov,[1] Harry B. Radousky,[2] Michael R. Armstrong,[2] Sarah K. Roberts,[2] and Jonathan W. Plaue[2]

[1)] *Geophysical Laboratory, Carnegie Institution of Washington, Washington, D.C., USA*

[2)] *Lawrence Livermore National Laboratory, Physical and Life Sciences Directorate, P.O. Box 808 L-350*

(Dated: 17 February 2015)

Pressure dependent angle-dispersive x-ray powder diffraction measurements of alpha-phase aluminum trifluoride (α-AlF_3) and separately, aluminum triiodide (AlI_3) were conducted using a diamond-anvil cell. Results at 295 K extend to 50 GPa. The equations of state of AlF_3 and AlI_3 were determined through refinements of collected x-ray diffraction patterns. The respective bulk moduli and corresponding pressure derivatives are reported for multiple orders of the Birch-Murnaghan (B-M), finite-strain (F-f), and higher pressure finite-strain (G-g) EOS analysis models. Aluminum trifluoride exhibits an apparent isostructural phase transition at approximately 12 GPa. Aluminum triiodide also undergoes a second-order isostructural rearrangement: applied stress transformed a monoclinicly distorted face centered cubic (fcc) structure into a standard fcc structural arrangement of iodine atoms. Results from semi-empirical thermochemical computations of energetic materials formulated with fluorine containing reactants were obtained with the aim of predicting the yield of halogenated products.

[a)]E-mail E.S. stavrou1@llnl.gov

[b)]E-mail J.M.Z. zaug1@llnl.gov

I. INTRODUCTION

Metal trihalides are highly interesting materials, with applications that range from batteries[1,2] and solar cells,[3] to improving resistance to laser damage.[4] In addition to their use in catalysis,[5] it is well known that a number of metals, metal oxides, and halide materials have extraordinarily effective antimicrobial properties. Their use in energetic formulations targeted at destroying/neutralizing bio-agents is hampered by the limited knowledge of their behavior at detonation and post-detonation conditions.[6] Aluminum (Al) in particular is the metallic fuel of choice in most cases due to its high heat of combustion in oxygen and easy availability. Since the oxidation of Al in fluorine (F) may provide distinct practical advantages over oxygen oxidation,[7] it has generated considerable recent experimental and theoretical interest in the behavior of Al powders mixed with a fluorine-rich oxidizer such as Teflon.[7–11] For such an energetic mixture, the completion of chemical reactions yields condensed AlF_3 as an end product; other aluminized explosives or propellants with large fluorine content (e.g. from polymeric binders) are also known to produce AlF_3 upon detonation.[12] As a result, knowledge of the AlF_3 equation of state (EOS) is crucial in understanding and modeling reactive shock behavior that involves oxidation of Al to AlF_3.[11] Likewise, the EOS of AlI_3 is required when molecular iodine or iodinated compounds undergo oxidation with Al.

The crystal structure of aluminum trihalides is mainly affected by the ionic radius of the halide anion. In the case of AlF_3 and $AlCl_3$, where the halide anion has a small ionic radius, aluminum cations are 6-fold coordinated with the consequent formation of AX_6 octahedra[13,14] (Figure 1(a)). In contrast, $AlBr_3$ and AlI_3 form Al_2X_6 dimers, where Al cations are 4-fold coordinated (Figure 1(b)). AlF_3 crystallizes in the rhombohedral α- phase structure (SG: R-3c (167)) at ambient conditions and undergoes a phase transition to the beta phase near 460^0 C (SG Pm3m).[14–18] Aluminum cations are 6-fold coordinated by F anions, forming canonical AlF_6 octahedra linked by corner sharing. This structure can be viewed as a distorted ReO_3 structure due to the rotation of the octahedra around their three-fold axis, which decreases the symmetry from cubic to rhombohedral.[14] A comprehensive description of the different phases for AlF_3 is given by Konig *et al.*.[19] At ambient conditions AlI_3 crystallizes in a monoclinic structure (SG: P121/c1 (14)) with four formula unit per unit cell.[20] Within this structure, Al_2I_6 dimmers are formed through the sharing of a common

edge between two AlI_4 tetrahedra. The terminal Al-I bonds are shorter than the bridging bonds. A closer inspection of this structure reveals that the iodide atoms form a distorted face centered cubic sublattice (Figure 1(c)) with cell distances and angles at near-to-ideal cubic values. $AlBr_3$ crystalizes in the same crystal structure; however, Br atoms form a distorted hexagonal-closed pack (hcp) sublattice.[21]

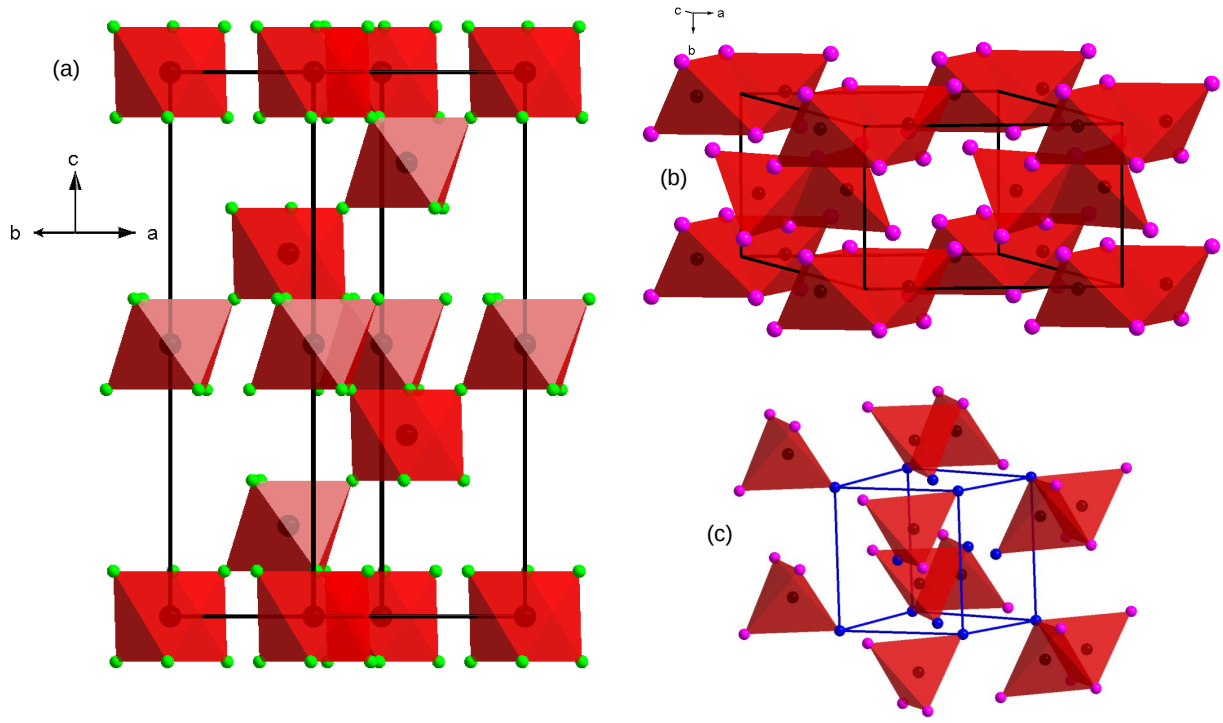

FIG. 1. Schematic representation of (a) rhombohedral AlF_3, aluminum and fluorine atoms are colored black and green respectively (b) Monoclinic AlI_3, aluminum and Iodine atoms colored black and light red respectively and (c) FCC-like Iodine atom arrangement in AlI_3, the Iodine atoms associated with the FCC-like cell are colored blue for clarity.

Here we have measured pressure dependent volume data for two candidate antimicrobial products, AlI_3 and AlF_3. Our aim is two-fold: first, the EOS data will more effectively constrain semi-empirical thermodynamic calculations of equilibrium chemistry where these materials are present as detonation products, and thus allow their integration into thermo-chemical calculations.[22] Second, we provide the first high-pressure experimental solid-solid structural phase information on aluminum trihalides. There are additional materials aspects worth pursuing too. A recent high-pressure study of boron triiodide (BI_3)[23] concluded that a

high-pressure phase exists above 6.2 GPa that becomes metallic and superconducting above 23 and 27 GPa respectively. Yao and Klug[24] attributed the appearance of superconductivity to the coordination change from planar BI_3 monomers to B_2I_6 dimers *i.e.* isostructural to ambient phase of AlI_3. In this sense, there is additional motivation to explore the high pressure structural behavior of the metallic-like cation Al-trihalides. A recent theoretical study[25] of Al_2Br_6 suggests that a dimer to a two dimensional polymeric phase transition occurs at low pressure (0.4 GPa) followed by a metallic phase above 80 GPa.

II. EXPERIMENTAL

Commercially available (Sigma-Aldrich) 99.99% pure anhydrous AlF_3 and 99.999% pure anhydrous AlI_3 were placed inside an argon gas purged glovebox and ground to fine powder. The samples including pressure sensors were loaded into separate diamond-anvil cell (DAC)sample chambers. Rhenium gaskets (preindented to 40-45 μm thick using 400 μm culets) were used to radially confine the pressurized samples. Initial sample chamber diameters were nominally 150 μm. Silicone oil was utilized as a pressure-transmitting medium (PTM):it is relatively inert, easy to load, and does not exhibit Bragg diffraction peaks. MAR355 CCD detector were used to collect pressure dependence X-ray diffraction (XRD) data at the Advanced Photon Source GSECARS (sector 13, λ=0.3344) and at the Extreme Conditions XRD Beamline P02.2 (λ=0.2895) at DESY (Germany). The monochromatic x-ray beams were focused to a nominal spot diameter of 4μm. Pressure was determined using a known ambient temperature EOS of gold[26] and also calibrated ruby luminescence.[27] The maximum pressure uncertainty was less than 0.2 GPa at the highest pressure achieved in this study. At the highest pressures achieved in this study, the deviatoric stress within the PTM exceeds 3 GPa.[28] Powder diffraction patterns were integrated using the FIT2D2[29] program to yield scattering intensity versus 2θ diagrams.

Powder samples at ambient conditions were analyzed on a Bruker AXS D8 ADVANCE X-ray diffractometer equipped with a LynxEye 1-dimentional linear Si strip detector. DIFFRACplus Evaluation package Release 2009 software was used for the data analysis.The samples were scanned from 20-85^0 2θ. The step scan parameters were 0.02^0 step and 2 second counting time per step with a 15mm variable divergence slit and a 1.0^0 antiscatter slit. Samples were x-rayed with Ni-filter Cu radiation from a sealed tube operated at 40kV

and 40mA. X-ray reference material (CeO_2) was analyzed before and after the samples to ensure goniometer alignment. No peak shifts were observed in the reference material.

III. RESULTS

A. AlF_3

In Figure 2, we provide selected pressure dependent x-ray diffraction patterns of AlF_3 up to 49 GPa. All the observed peaks in this pressure range were indexed with the ambient phase rhombohedral structure. No structural phase transition was detected up to 49 GPa. However, as it can be clearly seen from Fig. 2, there are strong pressure dependent trends in the relative scattering intensity of several peaks up to 20 GPa. This observation indicates that pressure-induced changes occurred to the atomic positional parameters. Given that Al atoms belong to Wyckoff position (WP) with fixed positional parameters (6b:(0,0,0)), the before mentioned change should involve only fluorine atoms at WP 18e. Structural parameters at different pressures together with ambient-pressure parameters are summarized in Table I. All structural parameters have been determined by performing full Reitveld refinements on each diffraction pattern using the GSAS program.[30] At 49.2 GPa the refinement residual values are Rp=6.5% and W_{RP}=8.5% at the highest pressure. An example Reitveld refinement (28 GPa) is shown in Figure 3(a).

TABLE I. Structural parameters of AlF_3 at six selected pressures: lattice parameters, unit-cell volume, and spatial coordinates for fluorine atom in the 18e(x,0,1/4) Wyckoff site. The special position for the aluminum cations is 6b(0,0,0).

P(GPa)	a (Å)	c (Å)	V_CELL s (Å^3)	x	y	z
0	4.9295 (8)	12.4456 (7)	261.91(1)	0.4275(2)	0	0.25
1.4	4.877(2)	12.418(2)	255.71(2)	0.406(2)	0	0.25
18.3	4.379(3)	12.399(3)	205.91(4)	0.364(3)	0	0.25
30.3	4.276(4)	12.211(4)	193.36(9)	0.354(4)	0	0.25
39.1	4.239(5)	12.122(4)	188.64(10)	0.358(5)	0	0.25
49.3	4.191(7)	11.96(5)	181.93(15)	0.352(7)	0	0.25

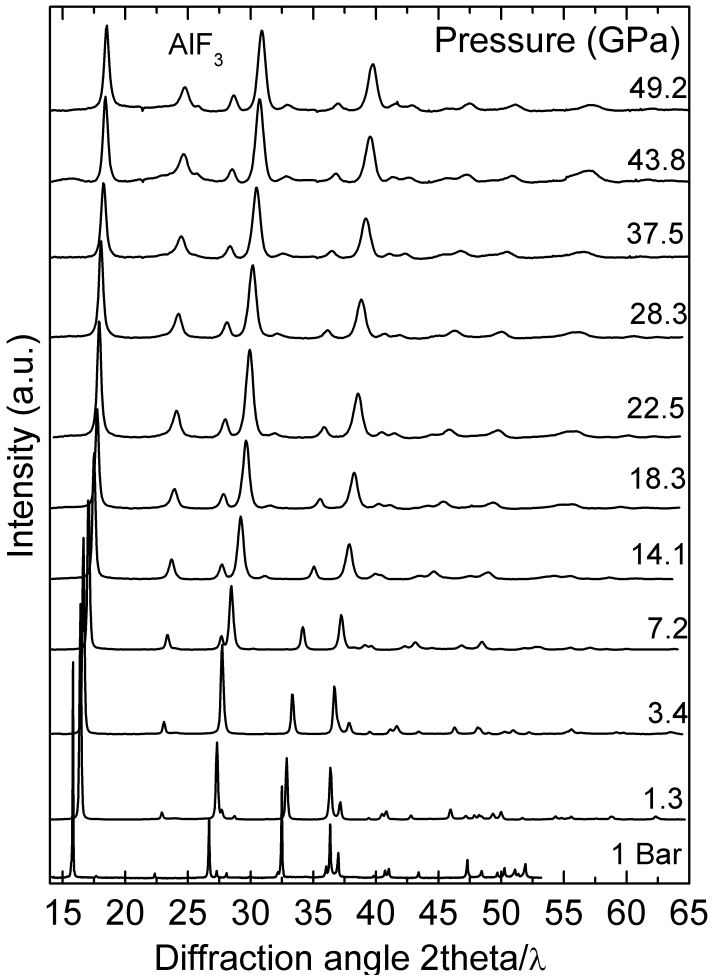

FIG. 2. Eleven selected pressure dependent X-ray diffraction patterns of AlF_3. The patterns are plotted as intensity versus $2\theta/\lambda$ because three different x-ray wavelengths were used.

The pressure dependent lattice parameters and unit cell volumes for the compression cycle are shown in Figure 4 (a) and (b) respectively. As can be clearly seen in Fig. 4 there is an apparent difference of the pressure behavior of the axes below and above ≈10 GPa. Below 10 GPa c-axis does not decrease with pressure, in contrast remains constant or even increases. Above 10 GPa, the c-axis starts to decrease with increasing pressure. On the other hand, the a-axis shows the opposite trend *i.e.* high compressibility < 10 GPa and measurably lower compressibility above this pressure. The changing pressure behavior of the axes is reflected in the a/c ratio (see inset of Fig. 4(a)).

In-line with most high-pressure EOS studies, we conducted unweighted fits of the pressure-volume data using a third-order Birch−Murnaghan (B-M) equation of state.[31]

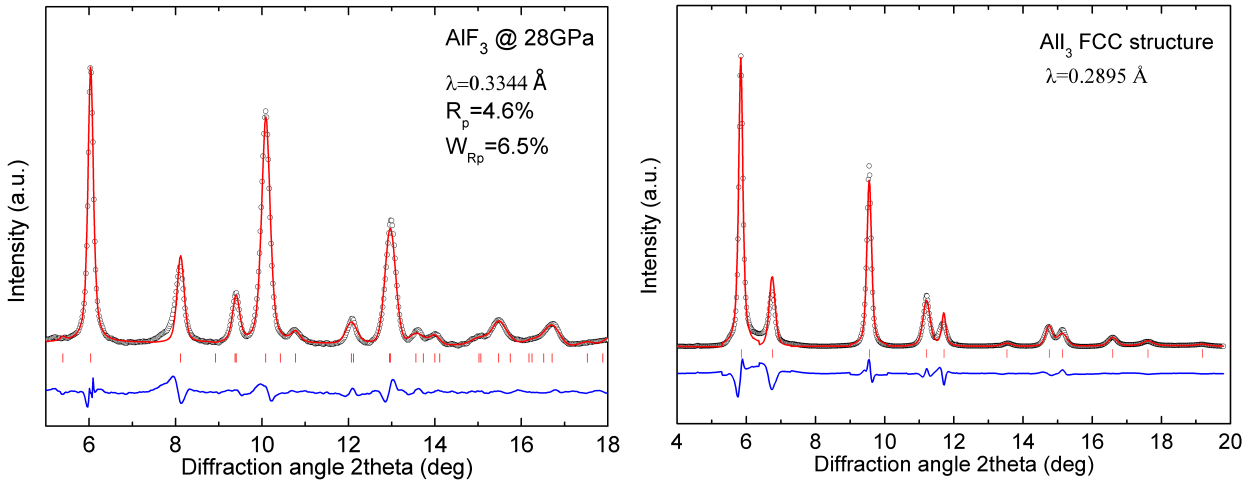

FIG. 3. (a) Rietveld refinement of AlF_3 at 28 GPa and (b) Le Bail refinement of AlI_3 at 26.3 GPa.

We determined the ambient pressure bulk modulus K_0 and the first pressure derivative K' for the low and high pressure phases independently and also for the entire pressure range (figure 4b). The results are as follows: (a)K_0=39 ± 8 GPa and K'$_0$=5.8 ± 2.5 for Phase I, (b) K_0=163 ± 15 GPa and K'=7.2 ± 2 for Phase I' and (c) K_0=19.5 ± 5.4 GPa and K'=15 ± 5 for the complete pressure range.

In order to gain deeper insight into AlF_3 response to static compression, we performed weighted fits and used the reduced χ^2_{red} goodness-of-fit formalism to compare the effectiveness of three EOS models to represent the P-V data. The reduced χ^2_{red} value closest to 1 represents the "winning model". For ambient pressure crystal structures, we applied the Birch-Murnaghan,[31] (B-M), 2^{nd} to 5^{th} orders, the Vinet,[32] and the F-f[33] finite strain 1^{st} to 3^{nd} order EOS models. For high-pressure crystal structure phases where V_0 is unknown, we replace the F-f model with the G-g model.[34] For each winning (best fit) model, where appropriate we plot corresponding two-dimensional confidence ellipses to reveal two-variable correlation information. Bivariable confidence plots enable a more comprehensive basis for comparison of EOS parameters to alternative theoretical and/or experimental results.[35]

The χ^2_{red} function is used with the assumption that measured values have uncorrelated Gaussian distributed error. For the case of a small number (N < 100) of data points, (like most high-pressure EOS studies), the uncertainty of χ^2_{red} values can be unacceptably large; moreover, for nonlinear fitting forms such as higher order EOS models, the "hat" matrix does not exist. In other words, there is no reliable means to compute the number of degrees

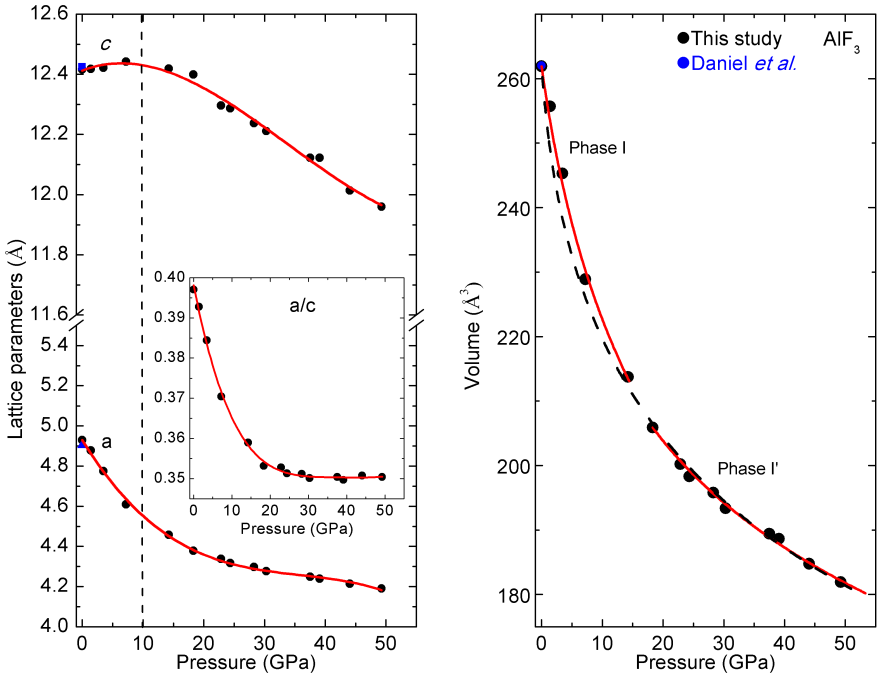

FIG. 4. Pressure dependence of (a) lattice parameters and (b) cell volume of AlF_3. The pressure dependence of the a/c ratio is plotted in the (a) inset. The solid red curves in (b) are the third-order Birch-Murnaghan EOS fit to the low and high pressure data ranges. The dashed black line shows a single equation of state fit for the entire low- and high pressure data. The blue symbols plotted at 0 GPa are from Daniel *et al.*[14]

of freedom, (NDF) for parameters in a nonlinear model; and further, NDFs can vary during an optimization search for a global minimum solution. For these reasons, we also conducted Kolmogorov-Smirnov tests[36,37] (KS-test), *i.e.*, compared converged model fit residuals to a Gaussian distribution with a mean value μ= 0 and a variance of σ^2 =1. The bias (highest region of sensitivity) of a KS-test is selected by the comparative Gaussian mean value distribution value. In some reports, the KS-test has been proven to be more robust than the reduced χ^2_{red} formalism.[38] KS-test values range from 0 (optimal) to 1 (poor).

When applying the F-f model to all of the AlF_3 data plotted in normalized pressure (stress) vs. Eularian strain units, it is quite apparent that there is a marked change in compressibility occurring between 10 and 15 GPa (See Figure 5a). There is an inflection point where the first 4-5 pressure points yield a negative K' where then the remaining data yield a positive trending K'. Curvature in F-f plotted results normally signals that a higher-order EOS is necessary to approximate the data. Moreover, a negative K' cannot be

attributed to a physical material. When a negative pressure derivative is derived through parameterization of an EOS model it usually is an indication that stress is being reduced through a structural phase transition where mixed crystalline phases co-exist or because there is an ensuing isostructural phase transition. (Isostructural transitions are often subtle and difficult to identify in P-V plotted data; discontinuous changes to pressure dependent cell volumes can be on the order of 1% or less than the experimental error[39]). Analysis of the AlF_3 diffraction data indicates that the latter process occurred. Therefore, we opted to fit AlF_3 data in what we will refer to (for the sake of brevity) as the low pressure phase-I (P<≈12 GPa) and the high-pressure phase-I' (P>12 GPa).

In the case of Phase-I, the third-order B-M model χ^2_{red} is an order of magnitude lower than the second-order model and so it better approximates the nature of the data. The third-order B-M and Vinet model experimentally weighted data fits, using pressure and volume estimated standard deviation, (esd), values, yield negative pressure derivatives. Because the F-f model phase-I data exhibit linear (non-varying) pressure dependence, it is plausible that the B-M and Vinet EOS models cannot appropriately represent the experimentally weighted data. The lower χ^2_{red} and Max ΔP of the Vinet model would seem to indicate that it more optimally approximates the data. Consequently, the Vinet EOS parameters serve as initial guess inputs for subsequent F-f model fits of the experimentally weighted phase-I data. The first-order linearized Eularian strain F-f EOS model yields positive K' values, regardless of the type of employed error weighting. The rate of changing compressibility of phase-I appears to be slow. The F-f model appears to generate the most satisfactory representation of the AlF_3 phase-I data. We show the first-order F-f model fits, to experimentally weighted and unweighted data, including the third-order B-M and Vinet model fits in Figure 5b. The EOS parameters derived from these fits are given in Table II. We also conducted a χ^2_{red} versus V_0 optimization search using the first-order F-f model. The resultant EOS values are Vo = 263.17(3) and K' = 46.5(6). The χ^2_{red} value for this fit is 1.04, the KS-test value is 0.30, and the maximum pressure difference between the data and the model is 0.61 GPa.

We next discuss the phase-I' AlF_3 EOS parameters. Because the V_0 value for phase-I' is unknown, we replace the F-f model with a corresponding linearized G-g stress-strain model where an arbitrary reference V_0 value is first chosen. The ambient pressure EOS parameters are determined at $g = g_0$ (strain at ambient pressure) using the G-g relation.[34] The most unambiguous result from applying these EOS models is that the Vinet model

TABLE II. The most optimal EOS model weighted fits for AlF_3. Note: K" is implied for B-M 2^{nd} order, Vinet and F(f) 1^{st} order results (See: O.L. Anderson, 1995 Oxford Univ. Press)

AlF_3 Phase-I											
Vinet EOS	V_0	V_0 esd	K_0	K_0 esd	K'	K' esd	K"	K" esd	χ^2_{red}	Max ΔP	KS-test
1	261.9191	0.0264	57.9638	2.7057	-1.3227	0.9153	0.0130	0.0026	25.3080	0.1959	0.3246
F-f order	V_0	V_0 esd	K_0	K_0 esd	K'	K' esd	K"	K" esd	χ^2_{red}	Max ΔP	KS-test
1	261.9140	0.0300	53.0553	3.3623	0.7316	0.7074	-0.2130	0.0750	29.1487	4.3087	0.3333
AlF_3 Phase-I'											
B-M order	V_0	V_0 esd	K_0	K_0 esd	K'	K' esd	K"	K" esd	χ^2_{red}	Max ΔP	KS-test
2	234.1143	2.0785	108.8932	8.5078	4	0	-0.0357	0.0028	156.7054	3.7215	0.5555
G-g order	V_0	V_0 esd	K_0	K_0 esd	K'	K' esd	K"	K" esd	Chi^2	Max ΔP	KS-test
1	232.1669	2.3628	133.0877	1.6359	4	0	-0.0292	0.0123	212.4607	0.3324	0.4444

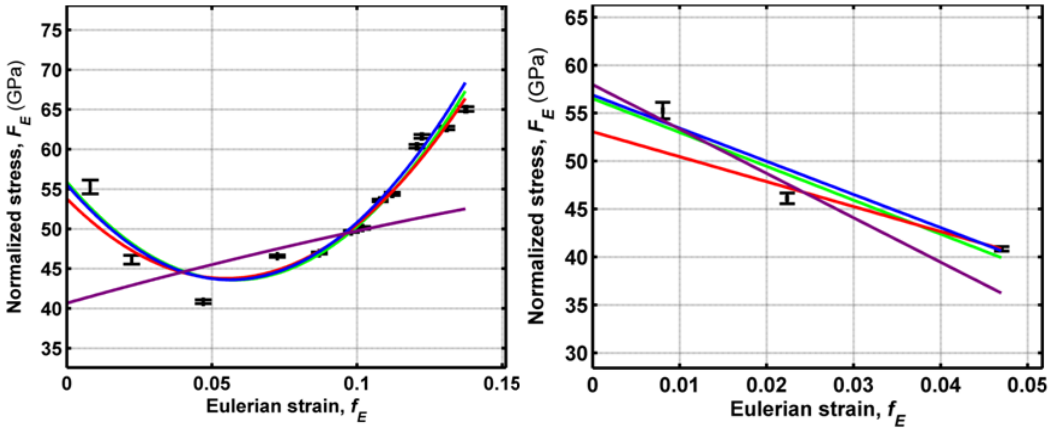

FIG. 5. a) All AlF_3 cold-compression data fit to a second-order F-f model. b) AlF_3 phase-I fit to a 1st order F-f model. Green lines represent unweighted fits and red lines are the experimentally weighted fits. Blue lines are a 3rd order B-M fit and violet lines are Vinet EOS model fits.

does not match well with the phase-I' data. Higher order Birch-Murnaghan fits, regardless of the data weighting scheme, are also poor facsimiles of the data and so here we present just the second-order fit parameters. Plotted results are provided in Figure 6. The G-g form of the data reveal that the lowest pressure point value at 14 GPa comprises a mixed phase material; the magnitude of its G-value lies measurably above a near-linear G vs. g trend established by the nine higher pressure data. We thus conducted a second-order B-M fit without the 14 GPa datum and made further comparisons. The equally weighted data errors are overestimated by the model as evidenced by a sub-linear χ^2_{red} value (0.32). The experimentally weighted data fit is statistically better than the fit including the 14 GPa

point. The same conclusion arises when applying the G-g model. Therefore, we report phase-I' EOS parameters from only the highest nine pressure points and thereby minimize fit parameter skewing effects induced by the incorporation of a mixed phase pressure point. The phase-I' V_0 value is 11.5 % less than the phase-I value and the phase-I' compressibility exceeds phase-I by 50%.

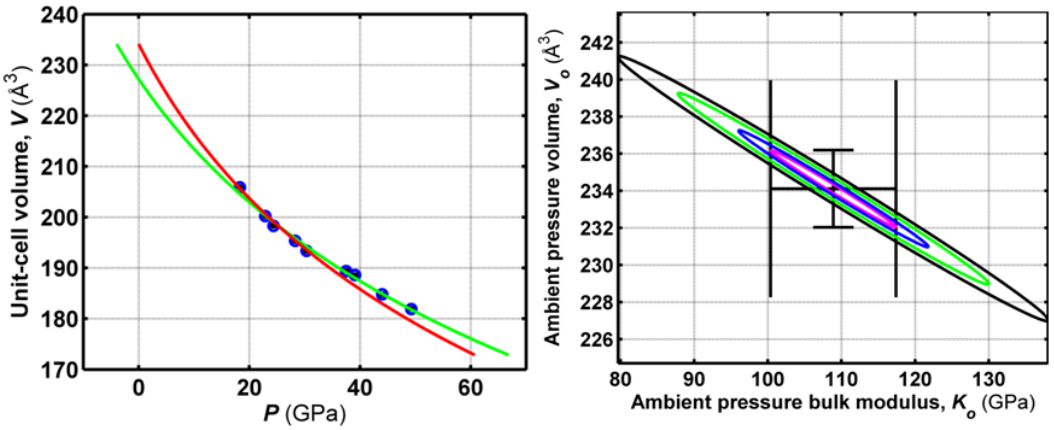

FIG. 6. a) AlF_3 second-order Birch-Murnaghan phase-I' fits (green line represents an unweighted fit and the red line is an experimentally weighted fit) and, b) The experimentally weighted fit confidence ellipses. The magenta colored ellipse is 0.607-σ (50.3% confidence), blue is 1-σ (68.3% confidence), green is 2-σ (95.4% confidence), and the black ellipse is 3-σ (99.7% confidence).

Although it may be plausible that the change in the slope of the pressure dependence of the lattice parameters, occurring at 10 GPa and the change of relative scattering intensity up to 20 GPa are related, it is difficult to make a definite conclusion. This is primarily because of the low Z of F atoms, since only F atoms are free to displace within the AlF_3 structure, which makes it difficult to systematically analyze (with confidence) Bragg diffraction peak intensities from DAC encapsulated samples. Nevertheless, our results suggest that with added pressure, F atoms continue to shift perpendicular to the c-axis (Figure 1(a)), which results in the anisotropic compression observed along different axes. A plot of the pressure dependent a/c axial ratio (Figure 4(a) inset) shows that this anisotropy holds to 20 GPa where then the ratio becomes invariant with pressure.

B. AlI_3

Nine selected pressure dependent XRD patterns of AlI_3 are shown in Fig. 7. There are no significant changes to the overall shape of the patterns up to 50 GPa. On the other hand, with increasing pressure, the diffraction patterns become simpler with the gradual decrease in the number of observed Bragg peaks. Doublet type peaks appear to merge into singlet peak shapes while the low intensity characteristic peaks of the monoclinic structure at low diffraction angles begin to are disappear. These observations suggest that the symmetry of the AlI_3 crystal structure increases. Indeed, the x-ray patterns at high pressures are representative of a simple face centered cubic (fcc) lattice. Taking into account that the high-Z iodine atoms dominate the x-ray scattering intensity, we conclude that iodine atoms are forming an undistorted fcc framework. So, under pressure, the distorted fcc framework of iodine atoms (see Fig. 1 (c)) is transformed to an undistorted framework, presumably through a second-order isostructural modification. Unfortunately the position of the aluminum atoms cannot be determined due to: i) experimental limitation of our measurements, mainly preferred orientation effects, and ii) the low Z-number of aluminum atoms in comparison to I atoms. Consequently, we are unable to comprehensively characterize the high-pressure phase of AlI_3 (this may ultimately be at task more suitable to theory) and refine the positional parameters as opposed to AlF_3. Our preliminary Raman measurements reveal that the-high pressure phase remains as a molecular solid without dissociation of iodine atoms. Further studies are needed to more fully elucidate the details of the pressure induced phase transition.

In order to determine the EOS of AlI_3, high-pressure patterns were refined (Le Bail) with a simple fcc iodine cell above 20 GPa. An example refinement for the 26.3 GPa pattern is shown in Figure 3(b). This cell cannot represent the actual unit cell due to the number of iodine atoms, 4 atoms per cell in the fcc lattice. For this reason, the volume of the fcc cell was normalized to the volume per formula unit (V_PFU) i.e. $V_PFU=3V_fcc/4$ following the same analysis used by Hamaya et al.[23] for the high pressure phase of BI_3. The pressure dependent V_PFU is shown in the plot of Figure 8. We conducted an unweighted fit of the pressure-volume data to a third-order Birch−Murnaghan equation of state[31] and determined the bulk modulus K_0=5.0(7) GPa and its first pressure derivative K_0=7.6(9). These values are representative of molecular crystals with weak connectivity between large molecules and

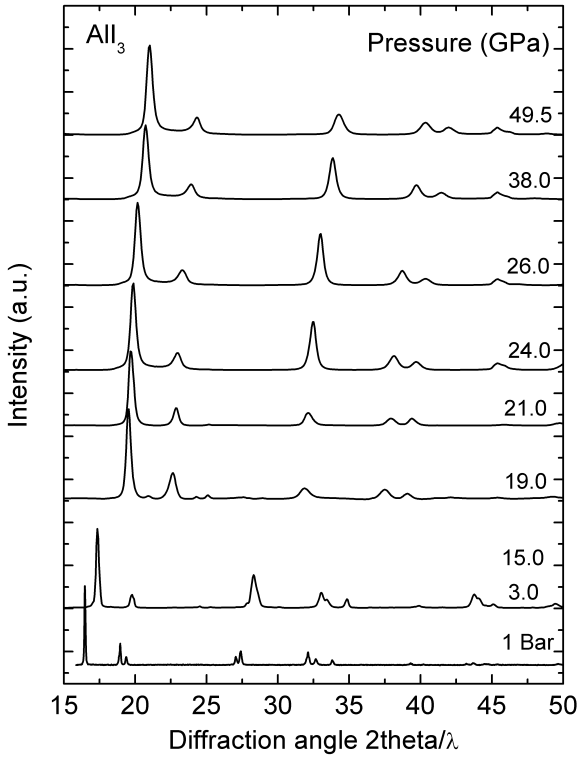

FIG. 7. Nine selected pressure dependent X-ray diffraction patterns of AlI_3.

in very good agreement with the reported ones in the case of BI_3.[23]

A survey of the pressure dependent AlI_3 data, plotted in F-f units, reveals a significant decrease in stress at pressures between ≈5-8 GPa, (strain between 0.11-0.16), followed by a near-linear positive increase in stress extending to 50 GPa (See: Figure 9a). We applied our EOS models to fit the low-pressure data below 5.1 GPa and found that the second-order B-M gave the most optimal representation of the data. The commensurate EOS parameters are given below in Table III. (See also Figure 9b.)

It would appear from the F-f plot in Fig. 8a that stress within the monoclinic crystal increases with applied strain until approximately 4 GPa, at which point the increased strain serves to release approximately 35% of the peak stress by 6-7 GPa. Perhaps a reasonable attribute for this phenomenon is that the iodine framework transitions from a distorted to an undistorted fcc structure. Indeed, from 9 to 50 GPa, lattice scale stress increases steadily with no further relaxation. Therefore, we fit pressure dependent data above 9.8 GPa where it appears a stable phase exists, albeit with an unknown structure.

The second-order B-M and the G-g first-order EOS models best approximate the high

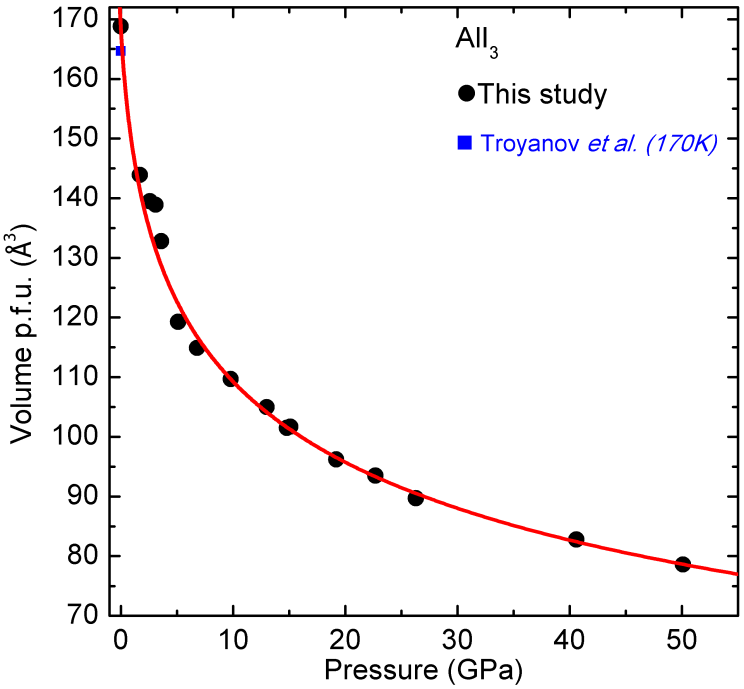

FIG. 8. Pressure dependence of volume per formula unit of AlI_3. Ambient volume at 170 K from Troyanov *et al.*[20] is plotted with blue square. The solid red curve is the third-order Birch-Murnaghan EOS unweighted fit.

TABLE III. Optimal EOS model weighted fits for AlI_3. Note: K" is implied for B-M 2^{nd} order, Vinet and Ff 1^{st} order results (See: O.L. Anderson, 1995 Oxford Univ. Press)

AlI_3 P < 5.1 GPa (Monoclinic lattice cell, distorted FCC iodine framework)											
B-M order	V_0	V_0 esd	K_0	K_0 esd	K'	K' esd	K"	K" esd	χ^2_{red}	Max ΔP	KS-test
2	168.8299	0.0012	9.4327	0.5167	4	0	-0.4123	0.0226	8.7670	0.3787	0.3000
AlI_3 P > 9.7 GPa (Unknown structure with a minimally distorted FCC iodine framework)											
B-M order	V_0	V_0 esd	K_0	K_0 esd	K'	K' esd	K"	K" esd	χ^2_{red}	Max ΔP	KS-test
2	140.4624	2.2845	24.3573	2.0566	4	0	-0.1597	0.0135	11.1293	4.6572	0.2969
G-g order	V_0	V_0 esd	K_0	K_0 esd	K'	K' esd	K"	K" esd	χ^2_{red}	Max ΔPd	KS-test
1	139.9597	2.0742	29.0043	0.3295	4	0	-0.1341	0.0115	15.5787	0.1258	0.4441

pressure FCC lattice cell data. Fit comparisons to the data for the 2^{nd} order B-M model are provided in Figure 10. The second-order B-M model yields more optimal low χ^2_{red} values. The fit parameter esd values from the third-order model are anomalously large because the uncertainties in the data are severely overestimated by the model. The B-M and G-g V_0 values ($\approx$ 140 Å^3) are approximately 16% less than the ambient pressure phase. The

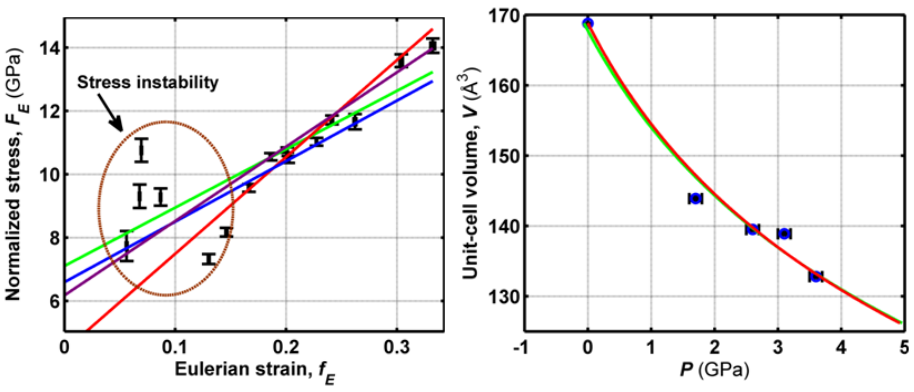

FIG. 9. a) All AlI_3 cold-compression data fit to a first-order F-f model. Green lines represent unweighted fits and red lines are the experimentally weighted fits. Blue lines are a 2^{nd} order B-M fit and violet lines are Vinet EOS model fits. b)Low pressure AlI_3 data fit using a second-order B-M model. Green line represents an unweighted fit and the red line is an experimentally weighted fit.

computed G and g errors are relatively low and thus lead to more significantly weighted differences between the model and the measured pressure. This is why the G-g model χ^2_{red} values are comparatively large despite the small maximum pressure difference from the data. The compressibility of the minimally distorted iodine FCC system is a factor of two less than the AlF_3 phase-I structure. Unfortunately, for logistical reasons we did not attempt to quench high-pressure materials back down to ambient conditions. Regardless, our EOS fits and commensurate interpretations can only be accepted accordingly as an attempt to optimally approximate the experimental data using relevant phenomenological EOS models. Our aim here has been to extract the most statistically correct thermodynamic parameters.

IV. DISCUSSION

The two end-members of aluminum trihalides (AlF_3 and AlI_3) examined in this study are remarkably stable: no first-order phase transition occurs up to ca 50 GPa. The pressure dependent response of AlF_3 lattice constants are remarkably similar to the general structural systematics of tetragonal 122 iron based superconductors (e.g. $BaFe_2As_2$ see ref.[40]). The main difference, beyond the cation coordination number, is the reverse behavior of axes, *i.e.* the c-axis shows high compressibility while the a-axis increases in 122 superconductors with-

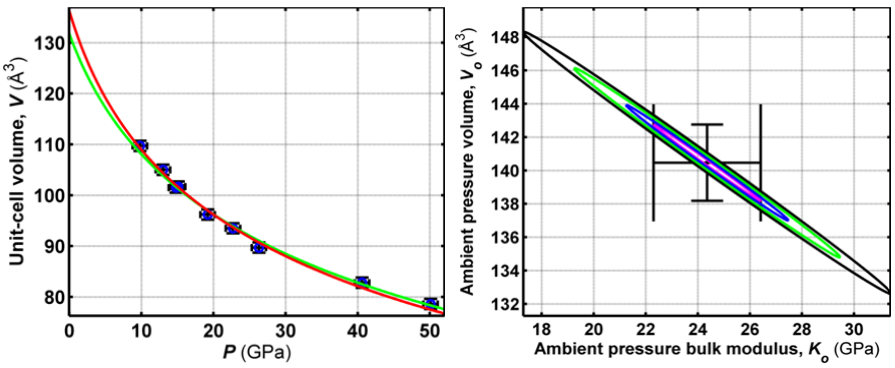

FIG. 10. a) AlI_3 second-order Birch-Murnaghan fcc lattice cell fits (green line represents an unweighted fit and the red line is an experimentally weighted fit) and, b) The experimentally weighted fit confidence ellipses. The magenta colored ellipse is 0.607-σ (50.3% confidence), blue is 1-σ (68.3% confidence), green is 2-σ (95.4% confidence), and the black ellipse is 3-σ (99.7% confidence).

out an abrupt change of volume. In this sense, we can use the term "collapsed rhombohedral" to describe the high-pressure modification of AlF_3 with the caveat that here "collapse" refers to the AlF_6 "layers" instead of the "stacking of layers ". One possible scenario lies in the interrelationship of the pressure dependence of the axes and the change of the relative intensities, *i.e.* both may have the same origin. The rotation of the AlF_6 octahedra units about the c-axis, as revealed by our Bragg peak refinements, serves to improve packing efficiency (approaching the ideal x/a=0.333 value for F with increasing pressure) and sequently to higher lateral compressibility. This mechanism is illustrated in figure 11. Further studies are needed to ascertain if this also affects electronic properties and the possibility of an underlying electronic phase transition.

A recent theoretical study on $AlBr_3$,[25] which is isostructural with AlI_3, reports a first-order phase transition from a molecular dimer to a planar polymeric phase at 0.4 GPa. This phase transition is accompanied by an increase of coordination number from 4- to 6-fold for Al atoms, *i.e.* formation of $AlBr_6$ octahedra, while the Br atoms maintain a hcp-like arrangement. As the authors discuss, an XRD experimental study will probably not detect general changes to the shape of diffraction patterns given the much higher Z of Br atoms, thus making the determination of Al position difficult. However, this phase transition is accompanied by an abrupt reduction (≈20%)of cell volume. In the case of AlI_3 the difficulty of determining Al positions is higher and so, a first-order phase transition cannot as yet

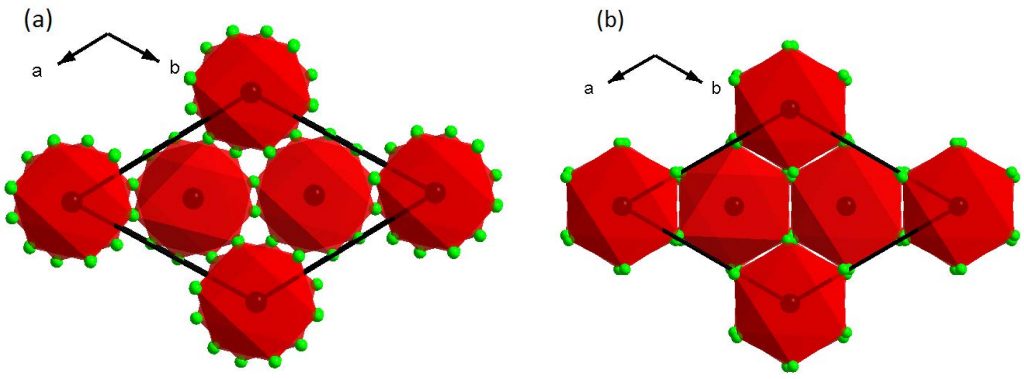

FIG. 11. Schematic representation of the rhombohedral AlF_3 with projection along the c-axis at (a) ambient pressure and (b) at 49 GPa.

be excluded by the fact that I atoms keep their fcc-like sublattice. One expects that AlI_3 will follow an $AlBr_3$-like phase transition at a measurably lower pressures. On the other hand, since no abrupt change of volume has been observed, it is reasonable to assume that AlI_3 retains a dimmer configuration. A more detailed XRD study combined with neutron diffraction is really needed to fully clarify the high pressure phase.

We turn our attention now towards the possible use of Al-trihalides as bio-agents, particularly through their production in the detonation of complex explosive formulations. The addition of metals, especially aluminum, to organic energetic compounds is a well-known avenue for increasing the energy content and performance of these materials for industrial and military applications, and therefore it remains a very active research field.[8,41–43] Aluminized explosive formulations with oxidizers containing fluorine and/or iodine are also currently being studied for potential use against bio-agents.[44] The thermochemistry of aluminum in the high pressure and temperature reactive environment characteristic of chemical detonations is not yet fully elucidated, especially for high halogen content. Experimental results obtained for Al-Teflon mixtures strongly suggest for example that such systems can sustain detonation,[9,10] which was speculated to be a largely "gas-free"process. To test this hypothesis theoretically, we integrated the equation of state of AlF_3, determined here from experimental data, into chemical equilibrium calculations[22] that also contain Al (liquid, solid) and carbon (diamond, graphite, liquid) as condensed products, and F_2, CF_4 and Al as gas products. These calculations yield classical Chapman-Jouguet[45] points with negligible gas content, but with detonation velocities almost an order of magnitude smaller than those pre-

viously reported.[10] Recent experimental work on Al-Teflon mixtures[7] indicates on the other hand that gas products containing both Al and F are likely to form under high temperature conditions. Consequently, we have also performed chemical equilibrium calculations that included AlF_3 as a gas product, since this is the lowest formation enthalpy molecule that includes both Al and F. The modeling of these gas species is however only approximate[46] due to the lack of experimental or theoretical data. Chapman-Jouguet calculations yield in this case detonation velocities approximately 50% higher than the experimental ones, with low amounts of condensed AlF_3.

Although the present estimates are not sufficiently accurate for drawing definitive conclusions, and moreover detonations in these systems are likely to be highly non-ideal processes,[11] the results suggest that gas products probably play a significant role in generating the observed reactive shock velocities in Al-Teflon and possibly other similar mixtures. Additional experimental and theoretical work is necessary to fully elucidate this issue. Nevertheless, knowledge of high pressure experimental EOS data of condensed AlF_3 and AlI_3 are key steps towards the realistic semi-empirical modeling of reactive shock and high pressure combustion processes that involve both fluorine and/or iodine and the oxidation of aluminum, *e.g.* encountered in high explosives detonation and subsequent expansion. The EOS data determined in the present study enables the development of thermochemical prediction tools that will guide the development of efficient bio-agent defeat energetic formulations by optimizing the production of chosen specific biocidal products at detonation conditions. By quantifying the temperature and pressure dependent release of halogen gases, formation of biocidal metal oxides, halides, etc., such thermochemical calculations, possibly coupled with suitable kinetic and hydrodynamic simulations, lays groundwork required for systematic approaches toward the chemical neutralization of biological agents.

V. SUMMARY

X-ray diffraction results are presented on both AlF_3 and AlI_3 to pressures of 50 GPa; no high-pressure experimental data have been previously available for these materials. AlF_3 has an interesting structural response signaled by the variation in peak intensities up to 20 GPa; however, there is no evidence of a structural transition. AlI_3 undergoes a second-order isostructural rearrangement that transforms the ambient pressure monoclinic distorted face

centered cubic structure into a standard fcc structure. The respective bulk moduli and corresponding pressure derivatives were derived from weighted and unweighted fits using various EOS models. These experimental EOSs improve the confidence of thermochemical modeling predictions of high pressure-temperature detonation reactions where aluminum trihalides are known products.

Notes

The authors declare no competing financial interest.

ACKNOWLEDGMENTS

We gratefully acknowledge support for this research by the Defense Threat Reduction Agency under contract number HDTRA1-11-1-4538I (program manager is Dr. Suhithi Peiris). This work was performed under the auspices of the U. S. Department of Energy by Lawrence Livermore National Laboratory under Contract DE-AC52-07NA27344. The research leading to these results has received funding from the European Community's Seventh Framework Programme (FP7/2007-2013) under grant agreement n 312284.

REFERENCES

[1]Y.-K. Sun, M.-J. Lee, C. S. Yoon, J. Hassoun, K. Amine, and B. Scrosati, Adv. Mater. **24**, 1192 (2012).

[2]W. Xu, X. Chen, W. Wang, D. Choi, F. Ding, J. Zhang, Z. Nie, Y. J. Choi, J.-G. Zhang, and Z. G. Yang, J. Power Sources **236**, 169 (2013).

[3]Z. Lan, J. Wu, J. Lin, and M. Huang, Electrochim. Acta **60**, 17 (2012).

[4]M. Mende, I. Balasa, H. Ehlers, D. Ristau, D.-B. L. Douti, L. Gallais, and M. Commandré, in *Optical Interference Coatings* (Optical Society of America, 2013) p. FA.5.

[5]G. Ertl, S. F. Helmut Knzinge, H and, and J. Jens Weitkamp, eds., *Handbook of Heterogeneous Catalysis* (Wiley-VCH, Weinheim, 1997).

[6]R. Pita, Toxin Rev. **28**, 219 (2009).

[7]R. W. Conner and D. D. Dlott, Chem. Phys. Lett. **512**, 211 (2011).

[8]E. L. Dreizin, Prog. Energ. Combust. **35**, 141 (2009).

[9]A. Y. Dolgoborodov, M. N. Makhov, I. V. Kolbanev, A. N. Streletskii, and V. E. Fortov, JETP Letters **81**, 311 (2005).

[10]A. Dolgoborodov, M. Makhov, I. Kolbanev, and A. Streletskii, in *13th International Detonation Symposium, Office of Naval Research* (2006).

[11]S. Yoo, D. S. Stewart, S. Choi, and D. E. Lambert, Shock Compression of Condensed Matter - 2011, Pts 1 and 2 **1426**, Amer Phys Soc (APS), Top Grp; Los Alamos Natl Lab; Lawrence Livermore Natl. Lab; Sandia Natl Labs (2012).

[12]D. L. Ornellas, "Calorimetric determinations of the heat and products of detonation for explosives: October 1961 to april 1982," Tech. Rep. (Ucrl-52821 Lawrence Livermore National Laboratory, 1982).

[13]J. Ravez, A. Mogusmilankovic, J. P. Chaminade, and P. Hagenmuller, Mater. Res. Bull. **19**, 1311 (1984).

[14]P. Daniel, A. Bulou, M. Rousseau, J. Nouet, J. L. Fourquet, M. Leblanc, and R. Burriel, J. Phys.: Condens. Matter **2**, 5663 (1990).

[15]R. Hoppe and D. Kissel, J. Fluorine Chem. **24**, 327 (1984).

[16]C. Alonso, A. Morato, F. Medina, F. Guirado, Y. Cesteros, P. Salagre, J. E. Sueiras, R. Terrado, and A. Giralt, Chem. Mater. **12**, 1148 (2000).

[17]F. Hanic and D. Stempelova, *Theory and Structure of Complex Compounds*, edited by B. Jezowska-Trzebiatowska (Macmillan: New York, 1964).

[18]P. J. Chupas, S. Chaudhuri, J. C. Hanson, X. Y. Qiu, P. L. Lee, S. D. Shastri, S. J. L. Billinge, and C. P. Grey, J. Am. Chem. Soc. **126**, 4756 (2004).

[19]R. Koenig, G. Scholz, K. Scheurell, D. Heidemann, I. Buchem, W. E. S. Unger, and E. Kemnitz, J. Fluorine Chem. **131**, 91 (2010).

[20]S. I. Troyanov, T. Krahl, and E. Kemnitz, Z. Kristallogr. **219**, 88 (2004).

[21]S. I. Troyanov, Zh. Neorg. Khim. **39**, 552 (1994).

[22]S. Bastea and L. Fried, in *Shock Waves Science and Technology Library, Vol. 6*, Shock Wave Science and Technology Reference Library, Vol. 6, edited by F. Zhang (Springer Berlin Heidelberg, 2012).

[23]N. Hamaya, M. Ishizuka, S. Onoda, J. Guishan, A. Ohmura, and K. Shimizu, Physical Review B **82**, 094506 (2010).

[24]Y. Yao, D. D. Klug, R. Martoňák, and S. Patchkovskii, Phys. Rev. B **83**, 214105 (2011).

[25]Y. S. Yao and D. D. Klug, J. Chem. Phys. **138**, 094501 (2013).

[26]M. Matsui, International Conference On High Pressure Science and Technology, Joint AIRAPT-22 and HPCJ-50 **215**, 012197 (2010).

[27]K. Syassen, High Pres. Res. **28**, 75 (2008).

[28]S. Klotz, J.-C. Chervin, P. Munsch, and G. L. Marchand, J. Phys. D: Appl. Phys. **42**, 075413 (2009).

[29]A. P. Hammersley, S. O. Svensson, M. Hanfland, A. N. Fitch, and D. Hausermann, High Pressure Res. **14**, 235 (1996), 4th Workshop of the IUCr High Pressure Group on Synchrotron and Neutron Sources, KEK, JAPAN, MAR 22-24, 1995.

[30]A. C. Larson and R. B. Von Dreele, "General structure analysis system (GSAS)," Los Alamos National Laboratory Report LAUR 86-748 (2004).

[31]F. Birch, J. Geophys. Res. **83**, 1257 (1978).

[32]P. Vinet, J. Ferrante, J. R. Smith, and J. H. Rose, Journal of Physics C-solid State Physics **19**, L467 (1986).

[33]F. Birch, Physical Review **71**, 809 (1947).

[34]R. Jeanloz, Geophysical Research Letters **8**, 1219 (1981).

[35]R. J. Angel, High-temperature and High-pressure Crystal Chemistry **41**, 35 (2000).

[36]A. Kolmogov, Giornale dell Istitutano degli Attuari **4**, 83 (1933).

[37]N. Smironov, Annals of Mathematical Statistics **19**, 279 (1944).

[38]G. Andrae, T. Schulze-Hartung, and P. Melchior, "Arxiv e-prints 1012.3754v1," (2010).

[39]S. M. Clark and J. M. Zaug, Physical Review B **82**, 134111 (2010).

[40]W. Uhoya, A. Stemshorn, G. Tsoi, Y. K. Vohra, A. S. Sefat, B. C. Sales, K. M. Hope, and S. T. Weir, Phys. Rev. B **82**, 144118 (2010).

[41]C. E. Johnson, T. J. Foley, and K. T. Higa, Multifunctional Energetic Materials **896**, Mat Res Soc; Lawrence Livermore Natl Lab; Nanotechnologies Inc; Office of Naval Research; Defense Threat Reduction Agency (2006).

[42]V. W. Manner, S. J. Pemberton, J. A. Gunderson, T. J. Herrera, J. M. Lloyd, P. J. Salazar, P. Rae, and B. C. Tappan, Propellants Explos. Pyrotech. **37**, 198 (2012).

[43]W. K. Lewis, C. G. Rumchik, M. J. Smith, K. A. S. Fernando, C. A. Crouse, J. E. Spowart, E. A. Guliants, and C. E. Bunker, J. Appl. Phys. **113**, 044907 (2013).

[44]C.Milby, D. Stamatis, J. Carney, J. Horn, and J. Lightstone, in *Proceedings of Central States Section of the Combustion Institute Spring Technical Meeting 2012Combustion Fundamentals and Applications, Dayton, Ohio, USA* (2012) p. 861.

[45]W. Fickett and W. C. Davis, *Detonation* (Univ. California Press, Berkeley, 1979).

[46]M. L. Hobbs, M. R. Baer, and B. C. McGee, Propellants Explos. Pyrotech. **24**, 269 (1999).